Geophys. J. R. astr. Soc. (1972) **31**, 45–66

Seismic Source Descriptions of Underground Explosions and a Depth Discriminate *

D. V. Helmberger and D. G. Harkrider

(Received 1972 August 21)†

Summary

Synthetic seismograms of both body waves and Rayleigh waves are used to determine the radiation field of a few large contained underground explosions. A number of possible source descriptions are investigated. A reduced displacement potential of the form, $\phi(t) = \phi_0 t^{\xi} \exp(-\eta t)$, fits the long- and short-period data. The source parameters appropriate for the Boxcar event are $\xi = 0{\cdot}5$ and $\eta = 0{\cdot}15$. Synthetic PL and Rayleigh waves are compared with observations from a number of different size events to determine the dependence of η on yield.

The amplitude of the long period synthetic body wave responses at ranges greater than about 12° increases rapidly as the source depth is increased. Thus the difference in spectral properties of explosions and earthquakes can be largely explained by the depth effect. The theoretical ratio SP/LP, that is the short period divided by the long-period amplitude, is computed from 12 to 25° for the Johnson upper mantle model and the Boxcar source. A study of an earthquake which cannot be distinguished from an explosion using the m_b *vs.* M_s criterion is investigated by the SP/LP discriminate.

Introduction

Recent studies of the m_b *vs.* M_s discriminate appear to be quite effective in separating nuclear events from earthquakes. After examining some of the events appearing in one such study (Liebermann & Pomeroy 1969), one sees why the method is so successful. Many earthquakes such as the Fallon earthquake (see Fig. 1) have very complicated source functions, that is the short-period time duration at transparent stations located in the north-east indicate at least 30 s of motion. Since the m_b measurement excludes most of the energy while the M_s does not, we see the merit of the method. However, there are other events with simple short-period sources that have relatively large M_s values, the low stress drop events. There are also simple earthquakes that have relatively small M_s, for example, the Oregon event (see Fig. 1) which will be studied in this paper.

One of the greatest difficulties in applying the m_b *vs.* M_s criterion is in determining m_b for small events. The problem is that amplitudes at range greater than 30° are very small, thus requiring amplitude information at nearer ranges. However, examining the recording between 12 and 30° one sees large variations as a function of

* Contribution No. 2152, Division of Geological and Planetary Sciences, California Institute of Technology, Pasadena, California 91109.

† Received in original form 1972 March 21

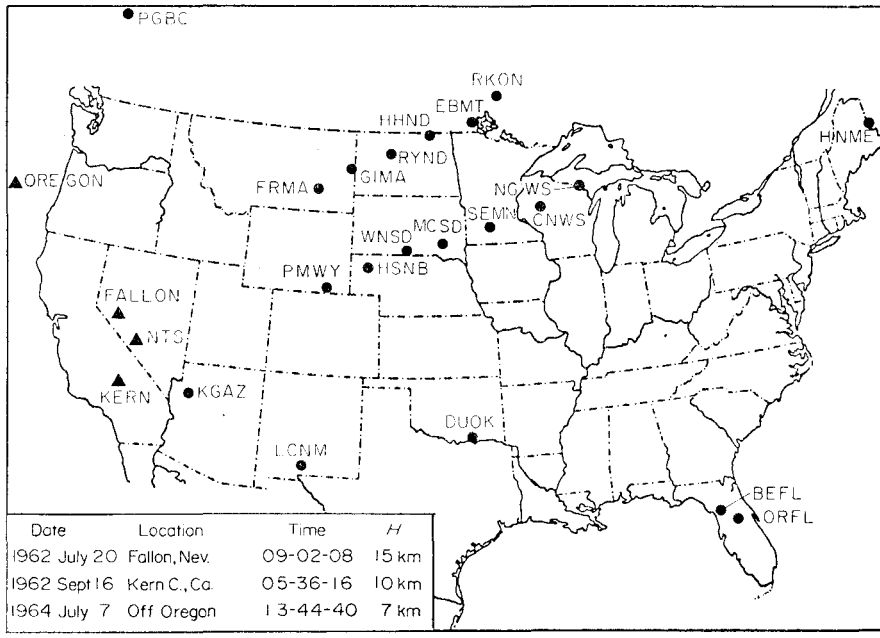

FIG. 1. Locations of events and LRSM stations.

range (see Helmberger & Wiggins 1971). Profiles of synthetic and observed seismograms are given in Fig. 2 to display the difficulty in measuring m_b. The amplitude of the first arrival is small and observed to have regional variations (see Wiggins & Helmberger 1972), except between 20 and 22° where it is strong and simple providing an excellent measure of m_b. In Fig. 3 we show the comparison of the 1964 July 7 earthquake, Oregon, with the Bilby explosion. The Oregon event was used in determining upper mantle structure and many of the short-period recordings are given in Helmberger & Wiggins (1971). The LRSM shot reports as well as our measurements made at calibrated stations indicate a m_b of 5·8 and a M_s of 4·3 for Bilby. The USCGS give the Oregon event an m_b of 5·7 and our measurements indicate an M_s of 4·3. A comparison of long-period vertical, LPZ, recordings are given in Fig. 4, also included is the observation from the explosion Handley. Note the small long-period P waves on the Bilby and Handley recordings while the corresponding earthquake arrivals are much larger. The m_b *vs.* M_s discriminate fails to separate these events but the ratio of short to long-period amplitude, SPZ/LPZ, is clearly different for these events. This relative enrichment of the long-period energy for earthquakes has been pointed out by Molnar (1971) and Wyss, Hanks & Liebermann (1971). We will develop the SPZ/LPZ dis riminate in this paper after a careful look at the source functions appropriate for explosions.

There has been much effort spent in determining the seismic radiation from nuclear explosions. The main effort has been in close-in experiments where the instruments are placed laterally from the source. Such measurements lead to parameterized descriptions of seismic fields (see Werth & Herbst 1963). One of the simplest descriptions in terms of yield and source rock type is given by Haskell (1967). The Haskell potential appears to be quite accurate with respect to short-period observations at distant stations; it is not good in predicting the long-period observations as we shall see. This is not surprising since the close-in data are limited to less than a second of onset. The approach followed in this paper is to determine the source

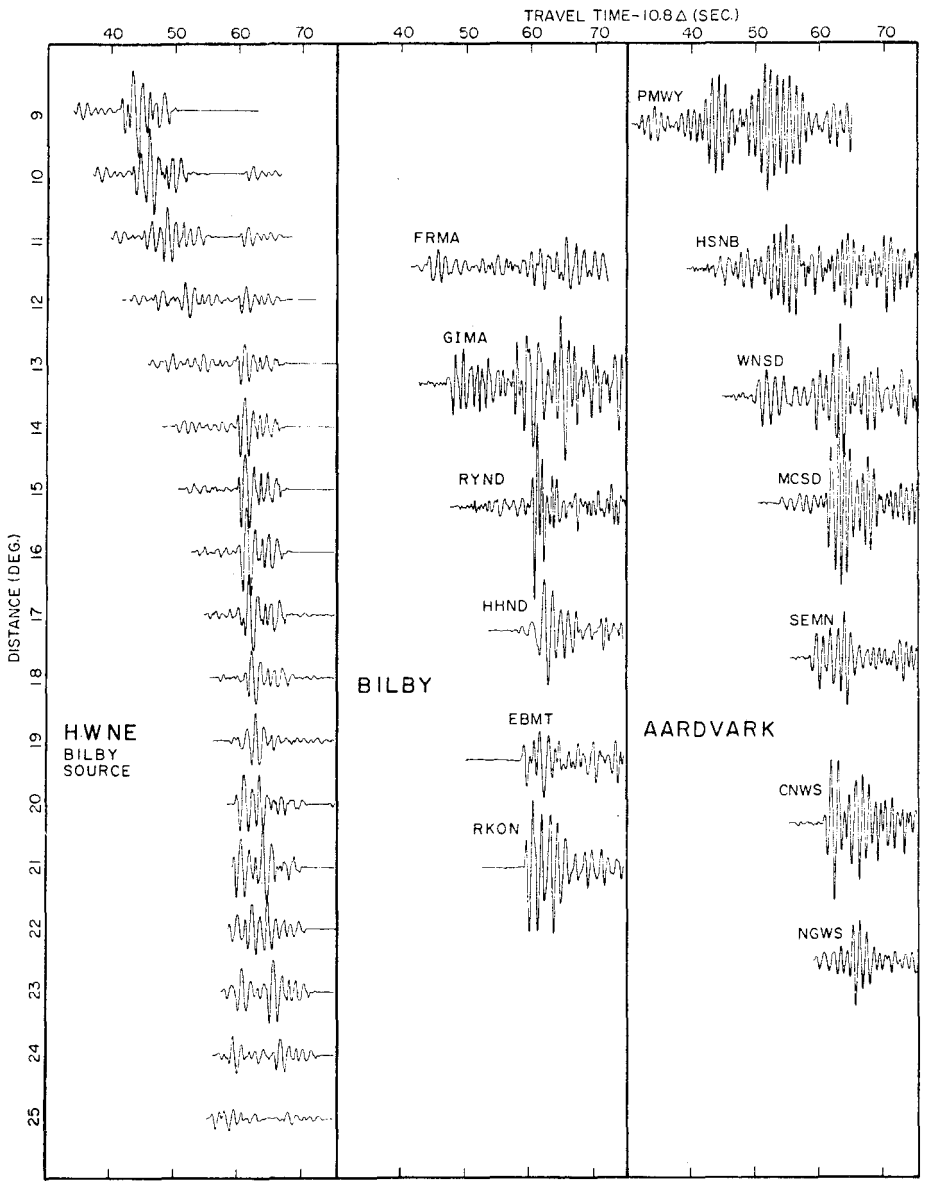

FIG. 2. Comparison of theoretical and observed seismograms.

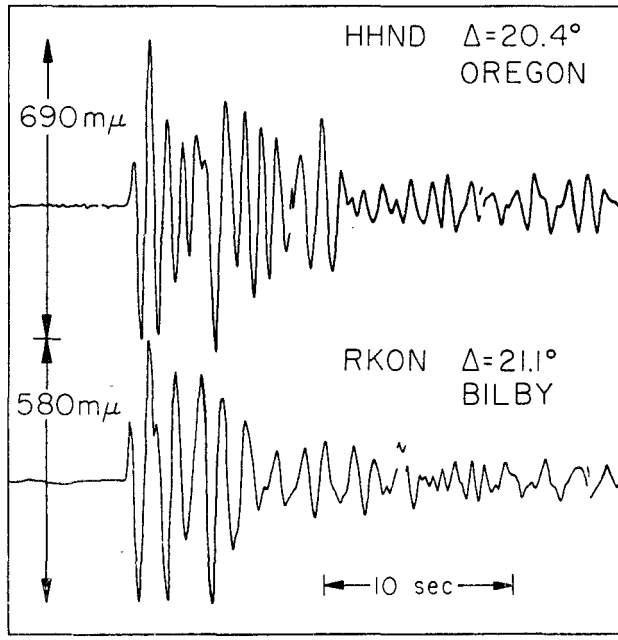

FIG. 3. Comparison of short period vertical observations from the Oregon earthquake and the Bilby explosion.

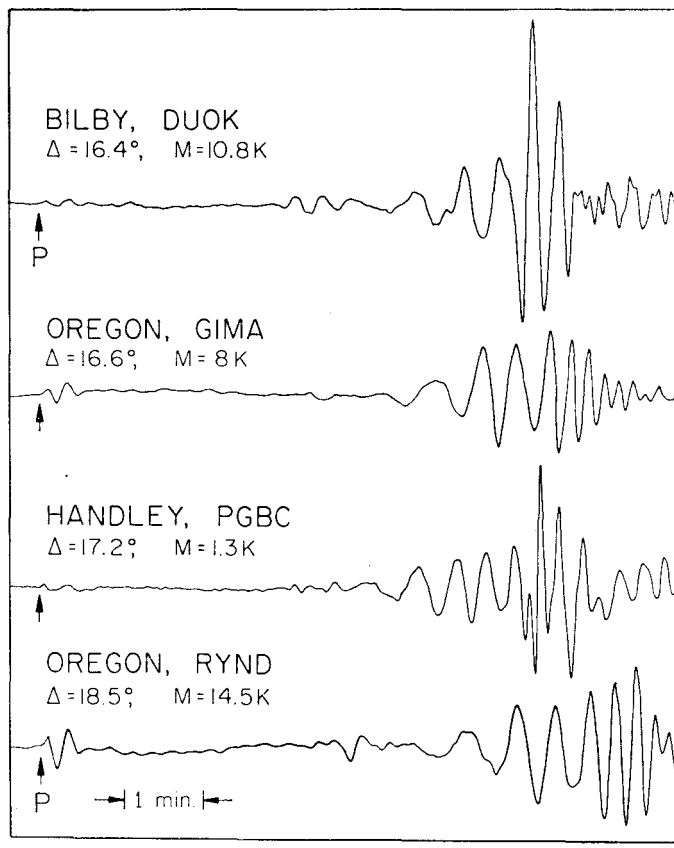

FIG. 4 Comparison of long-period observations from the Oregon earthquake and two NTS events.

function from distant short- and long-period LRSM observations. Using one of the recent upper mantle models one can generate synthetic responses for comparison with observations. The source parameters can then be adjusted by trial and error until the synthetics match the observations.

Synthetic and observed waveforms

The source function used in synthetic profiles such as Fig. 2 are obtained from supposed transparent stations beyond the upper mantle triplications. The LRSM observations in the eastern states will suffice for this purpose; example recordings are represented in Fig. 5. We can use these recordings for determinations of source shapes as pointed out by Carpenter (1967), Kogeus (1968) and others. However,

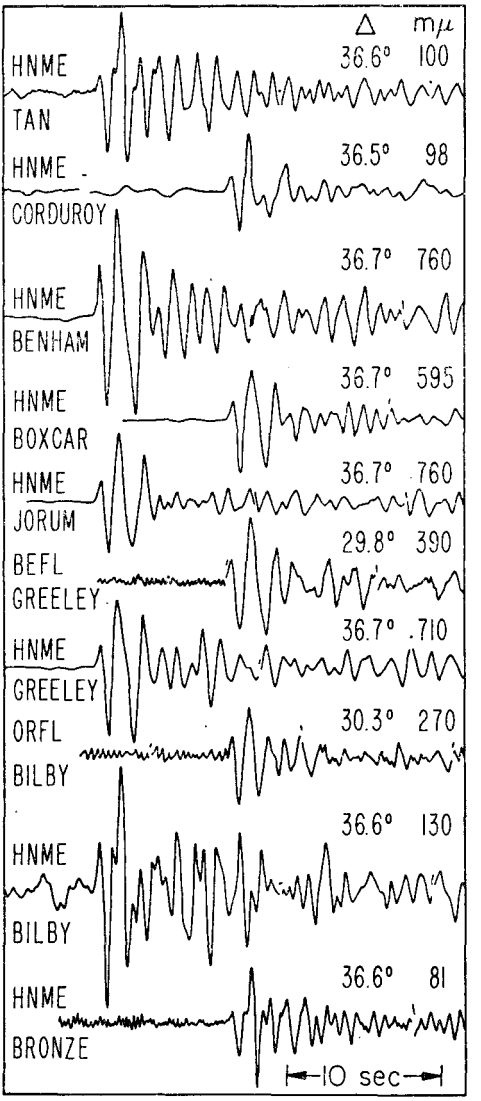

FIG. 5. Observations of various NTS events at relatively transparent stations. Zero to peak amplitude indicated above trace.

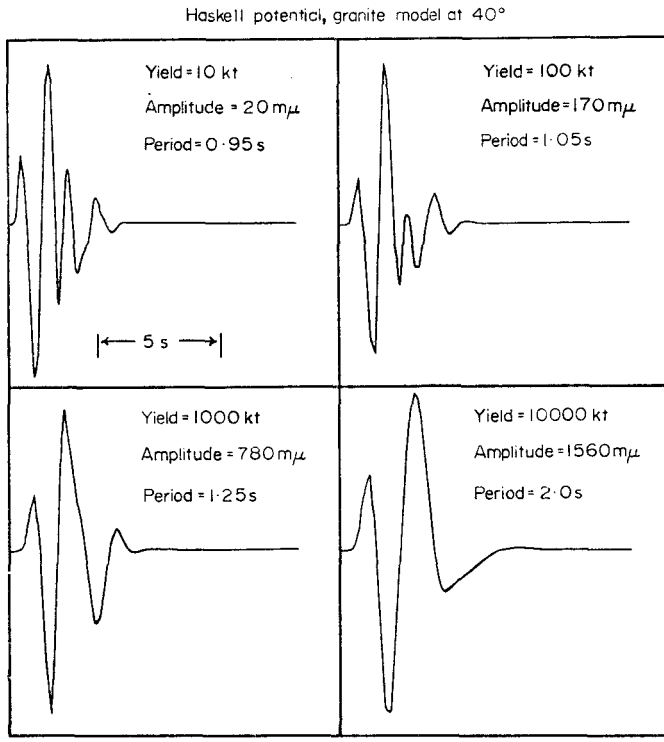

FIG. 6. Short period synthetic seismograms based on the Johnson model including P and pP and an absorption operator.

there is considerable azimuthal variations as can be seen in Fig. 5. Note that HNME is twice as large as BEFL for Greeley whereas the reverse is true for Bilby (see HNME and ORFL). This could be due to local structure at the receivers, but after studying many station pairs we think that amplitude variations of a factor of 2 are common in short-period source radiation patterns.

In constructing synthetic profiles for use in upper mantle inversion in previous studies we used a distant station such as HNME or ORFL as a standard. There is little need of an absolute amplitude scale in mapping triplication since only a relative measure is used. We now want to generate synthetic waveforms similar to those in Fig. 5 on the proper amplitude scale so that the synthetic seismograms given in Fig. 2 can be scaled in mμ. This will allow m_b measurements on synthetics as discussed in Harkrider & Helmberger (1972, in preparation). Using the crustal model given by Stauder (1971) and the Haskell displacement potential appropriate for explosions situated at a depth of 1 km we constructed the synthetics shown in Fig. 6, see the Appendix for a description of the method. Only the direct P and pP were included in this study since the observed pulses in Fig. 5 vary significantly after the first two seconds of motion and we are not particularly interested in modelling the surface properties at NTS. If we normalize P to unity then pP is about $-0{\cdot}9$ and pS is about $0{\cdot}3$. It would appear that the phase pP is sometimes seen as in HNME for Bilby and Bronze. The small down swing occurring about $0{\cdot}8$ s after the onset has the proper time for pP. In the generation of the synthetic waveforms in Fig. 6 we assumed an absorption operator (see Carpenter 1967) with $t^* = T/Q = 0{\cdot}75$. This has the effect of reducing the one-second amplitude level 80 per cent. The reason for adding this operator as indicated by Carpenter (1967) was to filter out the high frequencies (instrument peaks at 3 Hz) which in fact do not appear on the teleseismic records (see Fig. 5). We do

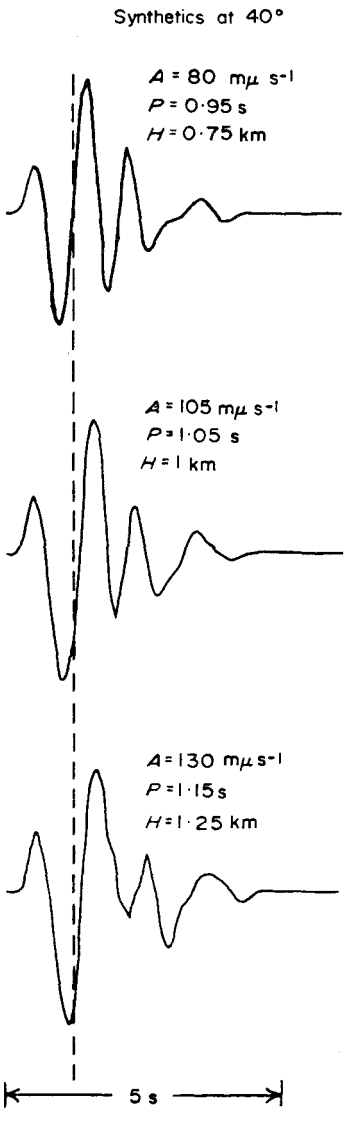

FIG. 7. Short period synthetics based on the Johnson model and the $\phi(t)$ potential assuming a 200 kt yield.

not know if this absence of short periods is due to scattering alone leaving the 1-s amplitude unaffected or if it is true absorption. We will assume the latter. We think that this attenuation comes about in traversing the low-velocity zone. Arguments to this effect will be set forth in a later paper. In this study we assume this attenuation to be independent of range, $t^* = 0{\cdot}75$ for all ranges, and confine our attention to SPZ's greater than 12°. Note that the amplitude in Fig. 6 does not scale directly as yield but increases somewhat slower. The change in period as a function of yield is apparent. There is also a change of period caused by the depth of source. The depth effect is displayed in Fig. 7 where we have used a new source function. Following Toksöz, Ben-Menahem & Harkrider (1964) we assume a displacement potential, $\phi(t)$, to have the following form

$$\phi(t) = \phi_0 t^{\xi} \exp(-\eta t).$$

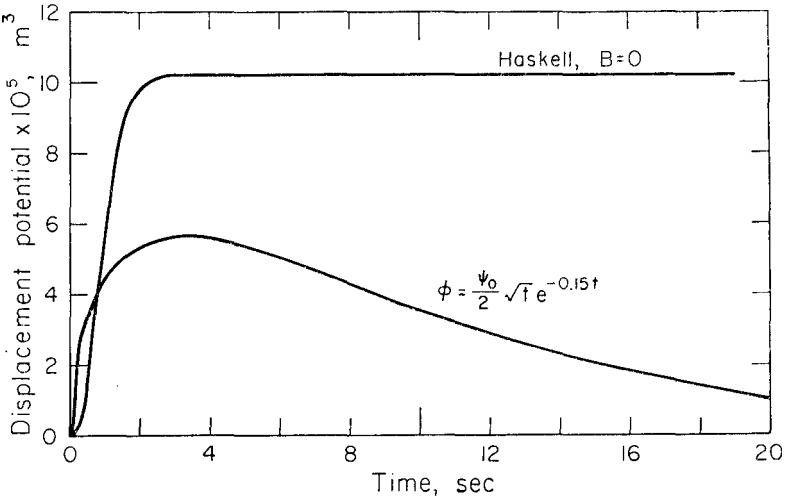

FIG. 8. Displacement potentials for a yield of a megaton.

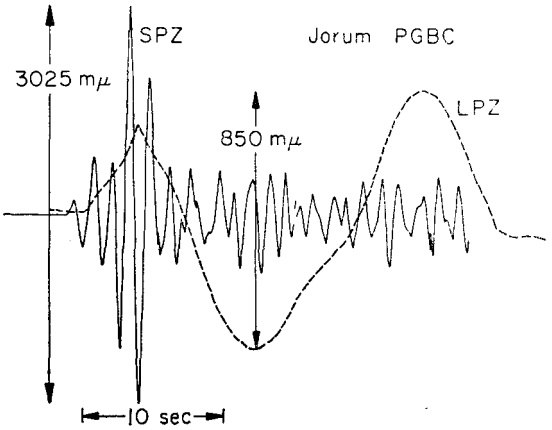

FIG. 9. Comparison between observed short- and long-period seismograms for Jorum.

We assume t to be expressed in seconds and that our expression is normalized with respect to time by dividing by $(s)^{\xi}$. With this assumption ϕ_0 is expressed in volume and can be set equal to ψ_∞ predicted by the Haskell formula. This expression with $\xi = 0{\cdot}5$ and $\eta = 0{\cdot}15$ and assuming a 200 kt source is used to obtain the pulses in Fig. 7. The values of ξ and η were derived from the Boxcar observations and will be discussed later (see Fig. 8 for a plot of $\phi(t)$ with $\phi_0 = \psi_\infty/2$ and Haskell potential).

The synthetic with $H = 0{\cdot}75$ is appropriate for Bilby. Note that its shape is much like ORFL and HNME in Fig. 5 and the relative amplitudes agree. This source sets the amplitude scale for the Bilby synthetics in Fig. 2. The amplitude of the large second arrival at 17° becomes 1100 mμ. The corresponding observed amplitude at HHND is 980 mμ. The m_b measured from the synthetics yields 5·8, the same as reported by the Bilby LRSM shot report. We emphasize that in calibrating the amplitudes in Fig. 2 we have used $\phi_0 = \psi_\infty$ and a yield of 200 kt.

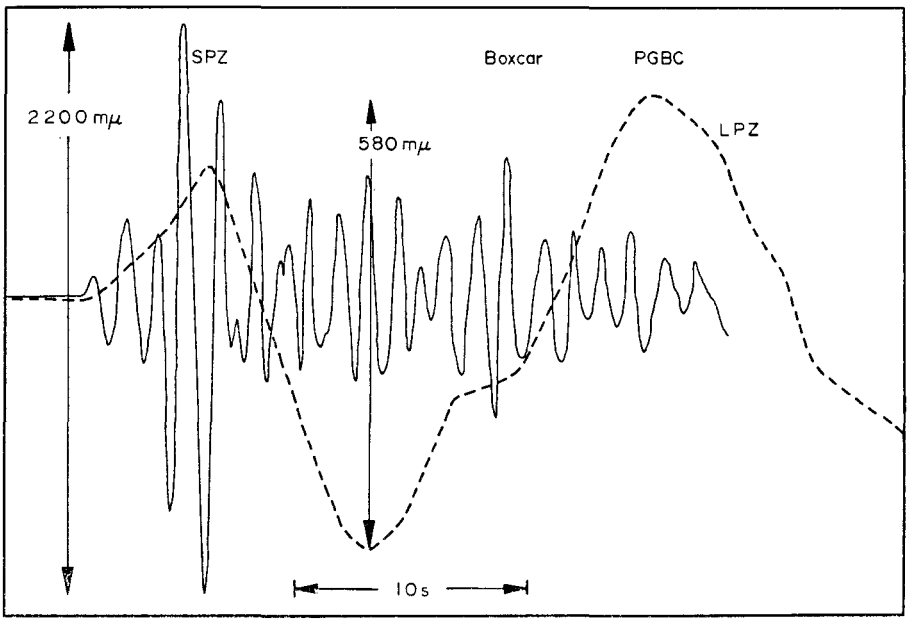

FIG. 10. Comparison between observed short- and long-period seismograms for Boxcar.

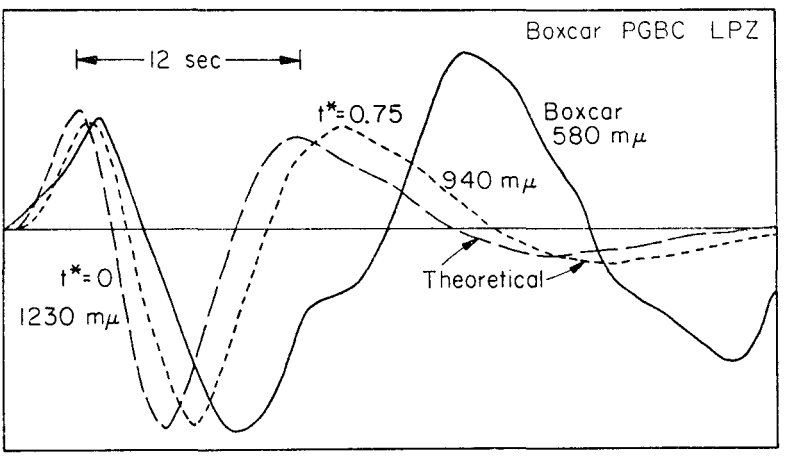

FIG. 11. Comparison of the Boxcar observation and the synthetic seismogram based on the Haskell potential ($B = 0$), with and without absorption.

By filtering out the high frequencies the SPZ measure becomes essentially a 1-s amplitude scale. To obtain more information about the source shape we must include the LPZ information which requires very large explosions. Unfortunately, most of the LRSM stations were discontinued before the megaton events were detonated. However, the remaining stations produced some spectacular records as indicated in Figs 9 and 10. The first arrival at this station is over 3 s late which explains the different appearance from the corresponding synthetics in Fig. 2 (see Wiggins & Helmberger 1972 for a discussion of lateral variation). The large second arrival is interpreted as coming from the 400 km transition zone and is near the expected arrival time. It also has the proper amplitude as compared to other LRSM stations. The LPZ amplitude is down by a factor of 4. Its dominant period is nearly 20 s.

Assuming the Johnson model we can easily compute the long-period synthetic for a specified potential with $B = 0$ (see Fig. 11). We generated the response with no absorption and with $t^* = 0{\cdot}65$. The addition of absorption does alter the waveform somewhat but is probably of the order of observational error. It would appear that a new source description is required. The comparison between the observation and the synthetic based on the Haskell potential indicates that the source function contains too much short-period energy. This is because LPZ depends on the derivative of the displacement potential and assuming a Haskell potential yields a smoothed delta function. Substituting other values of B does not solve the problem. The remedy is to take out the sharpness. Going back to the $\phi(t)$ potential introduced earlier we can examine the behaviour of synthetic SPZ and LPZ with respect to variations in ϕ_0, η, ξ. The parameter ξ controls the rise time and thus the SPZ response, whereas LPZ is strongly dependent on η. The parameter ϕ_0 is modelled after Haskell's ψ_∞. It is directly proportional to yield. Allowing these parameters to vary we can match the observed short- and long-period observations by trial and error. The best fit occurs for $\xi = 0{\cdot}5$ and $\eta = 0{\cdot}15$ and the intensity scaled to Haskell's $\phi_0 = \psi_\infty/2$ (see Fig. 8). Comparing the two source descriptions we note that the Haskell source has a smooth beginning, that is the first and second derivatives are constrained to zero. This is done to allow analytic energy considerations by truncating the very high frequencies. The radiated energy must remain finite. Since we have little information about these high frequencies (1-s recordings) we have not attempted to model this part of the curve. To make our source model more realistic at all frequencies would require the addition of a short ramp, the type used by Haskell would suffice. Our strategy is to use the model with the fewest parameters and still obtain adequate descriptions of observations beyond 12°, which we now demonstrate, realizing that our source model will not be adequate for high frequency observations. The comparison between the synthetic LPZ and the corresponding observation is given in Fig. 12. The time separation between P and pP, Δt, has a strong influence on the long period P waveform. This effect gives rise to the sharp onset which is apparent in Fig. 12. The amplitude of the 18-s energy is due to the normalized amplitude differences $(P-pP)$, which is about 0·1. As the depth is increased Δt grows and the period of the synthetic waveform decreases rapidly as its amplitude increases (see Figs 13 and 14).

A profile of long period vertical P and SV synthetics appropriate for the Johnson model are represented in Fig. 15. The shear velocity model is given in Table 1. It is based on travel-time inversion with the constraint that major discontinuities occur at the same depths as indicated by the P-data inversion. The model is not particularly unique but will suffice for our arguments concerning pS conversion. Only P mode generalized rays are used in computing the P waves and similarly only SV rays in SV generation. A brief discussion of this approximation is given in Helmberger & Morris (1970). The source of the SV motion is just the pS conversion at the surface. The SV synthetics in Fig. 15 display the strong interference caused by arrivals from the major transition zones. Constructive behaviour at 22° is quite spectacular. Strong

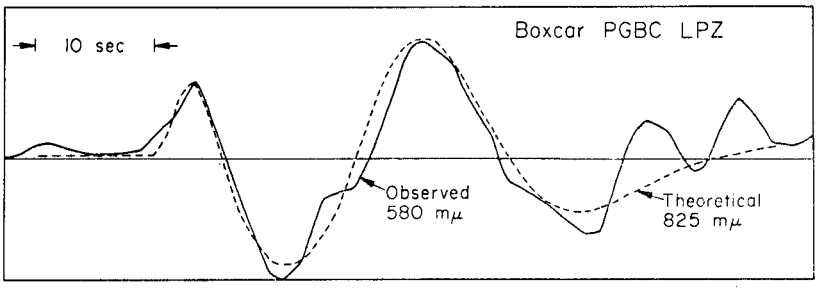

FIG. 12. Comparison of the Boxcar observation and the synthetic seismogram based on $\phi(t)$ from Fig. 8.

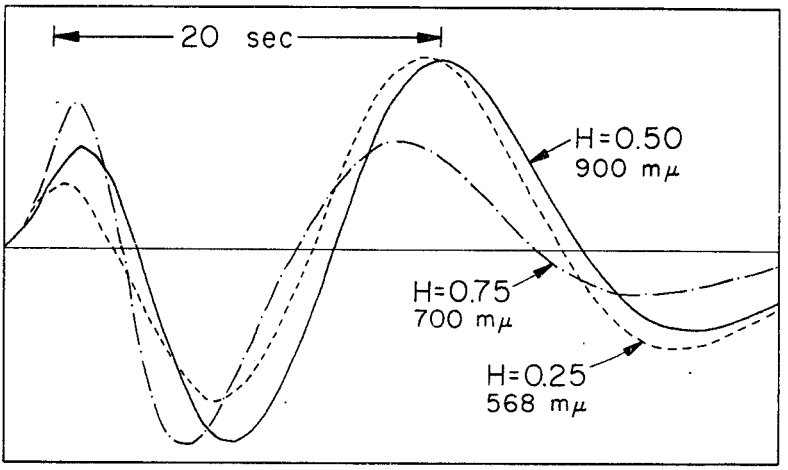

FIG. 13. LPZ's for $\phi(t)$ at different source depths.

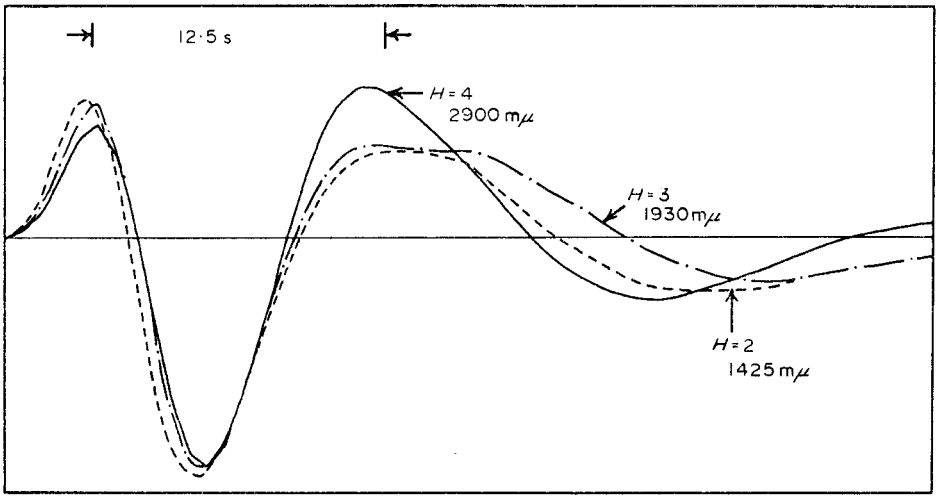

FIG. 14. LPZ's for $\phi(t)$ at different source depths.

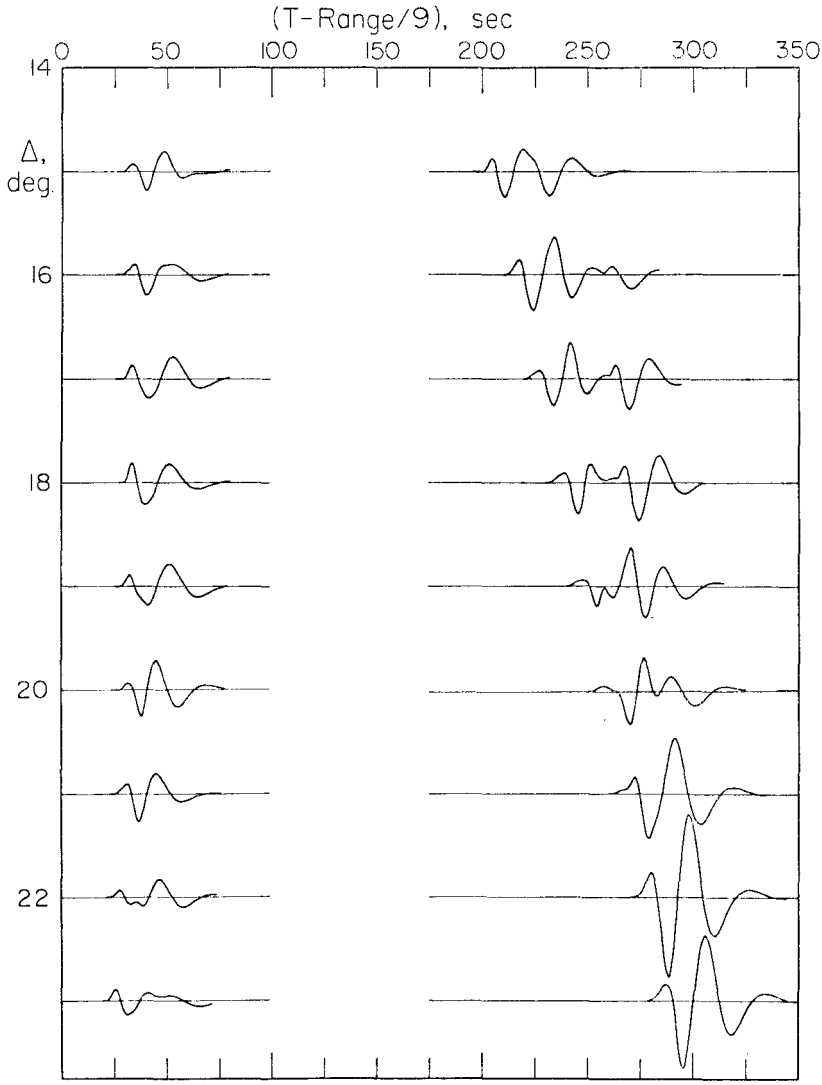

FIG. 15. Synthetic LPZ's based on $\phi(t)$.

destructive interference occurs at ranges less than 20° which looks much like the observations displayed in Fig. 4.

The upper mantle structure is also apparent in the synthetic P wave behaviour as displayed in Fig. 15. Note that the dominant period changes as a function of range. Assuming a different model such as HWNE produces similar waveforms at these ranges, since the large scale structural features are similar for these two models.

We expect from our previous discussion of $(P-pP)$ interaction that the long period P waves should behave as if the source was a composite of a delta function and step function, whereas the SV source should appear as a step. This effect is hardly discernible on the LRSM observations which are relatively narrow-band recordings. However, the above effect is displayed clearly by the broad-band WWSS stations where the SV waves appear distinctly larger and longer period than the corresponding P waves.

Table 1

Shear velocity profile

Radius (km)	Shear velocity (km s^{-1})	Radius (km)	Shear velocity (km s^{-1})
6371	3·50	5860	5·29
6331	4·50	5839	5·31
6316	4·60	5821	5·33
6304	4·60	5805	5·36
6257	4·50	5790	5·39
6234	4·50	5776	5·42
6209	4·40	5763	5·45
6197	4·50	5749	5·48
6189	4·53	5736	5·50
6185	4·78	5711	5·57
6170	4·80	5699	5·62
6157	4·8	5696	6·21
6114	4·81	5694	6·29
5960	4·82	5687	6·33
5936	4·86	5678	6·38
5932	5·07	5668	6·41
5929	5·15	5656	6·44
5923	5·19	5502	6·45
5911	5·22	5456	6·46
5896	5·25	5342	6·49
5879	5·27	5246	6·53

At shorter ranges the *P* wave merges with the *PL* wave. Assuming model II, the one-layer crust over uniform mantle discussed in Helmberger (1972) and the Boxcar source function we can compute a synthetic seismogram containing both *P* and *PL* as in Fig. 16. The periods are in fair agreement and again the synthetics are slightly large. Previous studies on the long-period spectra of source descriptions suggest that the parameter η is yield dependent, for example, Toksöz *et al.* (1964). It would be helpful to establish such a relationship by say fitting the long-period *P* waves for Bilby. However, the DUOK observation is the only station beyond 10° that gives any indication of the arrival and does not appear strong enough to merit study. Some insight into the problem can be obtained by comparing Boxcar with Bilby at LCNM. The ratio of the SPZ's for this station as well as the average for the entire network is 25 per cent, whereas the LPZ ratio is much smaller (see Fig. 17). The implication is that the exponential dropoff is indeed higher for Bilby.

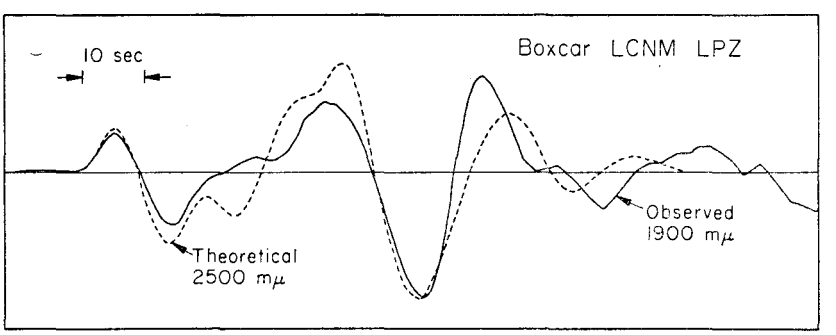

FIG. 16. Comparison between synthetic and observed *P* and *PL*.

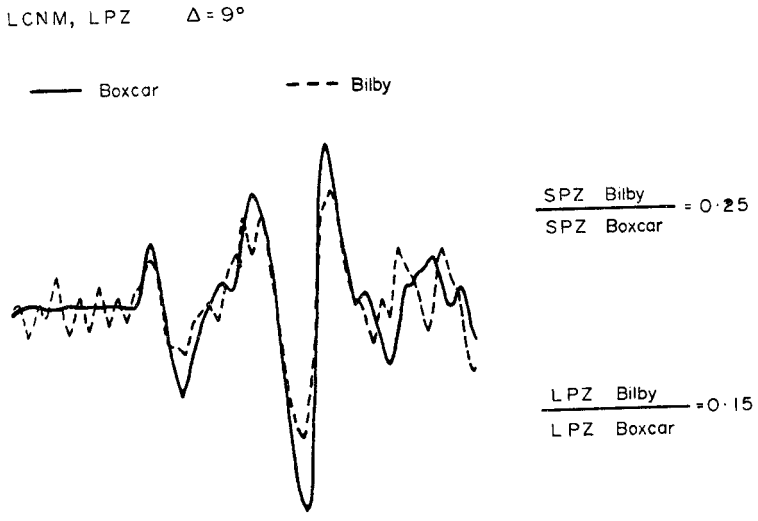

FIG. 17. Comparison of long period observations from Bilby (200 kt) and Boxcar (1000 kt).

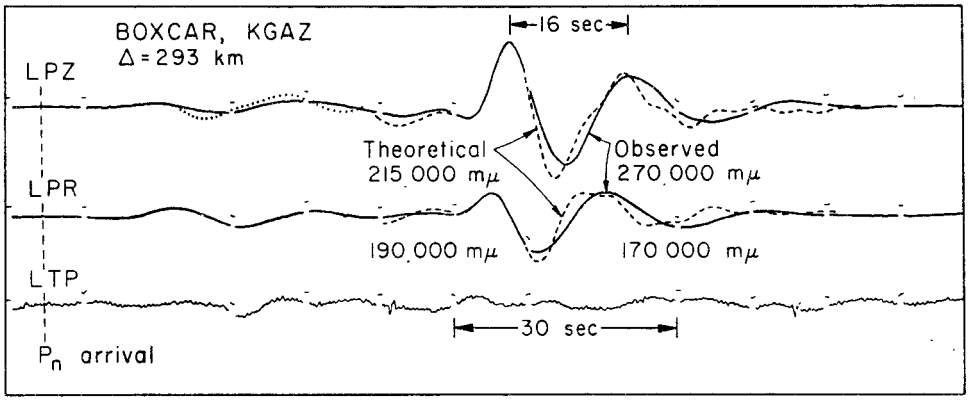

FIG. 18. Theoretical and observed seismograms at near range.

Table 2

Crustal model used in synthetic Rayleigh wave generation at 300 km

Layer	Thickness (km)	α(km s^{-1})	β(km s^{-1})	ρ(g cm^{-3})
1	0·96	2·7	1·6	2·0
2	0·37	3·4	1·9	2·2
3	0·81	3·8	2·1	2·3
4	0·36	4·4	2·5	2·4
5	2·5	5·1	2·6	2·5
6	20·0	6·1	3·5	2·7
7	10·0	7·0	4·0	3·0
8		8·0	4·6	3·3

As a further check on the reliability of our source function we compare the predicted Rayleigh waves with observations. To do this we chose the station KGAZ, $\Delta = 293$ km, since this profile from NTS has been studied by Diment, Stewart & Roller (1961) and found to have relatively simple structure (see Fig. 18). The long-period motion starting at the *Pn* time is the combination of *P* and *PL* as discussed by Helmberger (1972). We used model II to compute the synthetic (see the dotted plot in Fig. 18). Since there are numerous high-gain recordings of smaller events at these ranges, it would appear that just the *P* contribution, say the first 10 s, would be useful in source studies. We used the model given by Stauder (1971) based on the local NTS structure and the technique described by Harkrider (1964) in our theoretical Rayleigh calculations (see Table 2 for parameters). The comparison is displayed in Fig. 18. The apparent inverse dispersion is due mostly to the nature of the long-period LRSM response. We think the agreement is very good and consider our source function an adequate description of the Boxcar event.

Discriminating between earthquakes and explosions

In this section we return to the question of distinguishing explosions from small high stress-drop earthquakes. We approach the problem by supposing that some earthquakes have the same source function as Boxcar but occur somewhat deeper. We can then draw on the numerical experiments of the last section to predict the body wave behaviour. We will also examine the behaviour of Rayleigh waves as the depth is increased. After comparing these results with the problem earthquake, Oregon, we will discuss discriminates based on Rayleigh wave spectra and the SPZ/LPZ discriminate.

Examining Fig. 3 one can see little difference between the earthquake and explosion. It would not appear that *pP* can be identified and a focal depth determined for either event. However, looking at Fig. 4 we see striking differences. The longer periods are greatly enhanced in the earthquake records. We interpret this effect to be mostly due to the differences in source depth. This feature is demonstrated in Fig. 19, where we show the Rayleigh wave dependences on depth of source. The model was determined by the usual method of fitting the group velocity points with a dispersion curve and choosing the simplest model (see Table 3). We used the recordings from a number of large explosions in this determination. Since the LRSM instruments strongly attenuates periods longer than 40 s, there appears to be little influence by the mantle. The Rayleigh zero to peak amplitude of DUOK is 1100 mμ which agrees with the corresponding synthetics after correcting for yield, which is roughly a factor of 5. Increasing the source depth greatly attenuates the shorter periods as expected. It would appear that just the spectral ratio of say 10–30 s would be sufficient to distinguish this earthquake.

A somewhat simpler depth discriminate is the ratio of the short-period amplitude divided by the long-period amplitude, SPZ/LPZ. A plot of the theoretical ratio based on synthetic seismograms assuming the Johnson model and Boxcar source function is given in Fig. 20. We used the largest amplitudes on the short-period synthetics, taking advantage of the strong arrivals returning from the major transition

Table 3

Model used in synthetic Rayleigh wave generation at 1800 km

Layer	Thickness (km)	α(km s^{-1})	β(km s^{-1})	ρ(g cm^{-3})
1	1·5	3·00	1·40	2·60
2	28·0	6·15	3·55	2·74
3	10·0	7·00	4·00	3·00
4		8·14	4·70	3·30

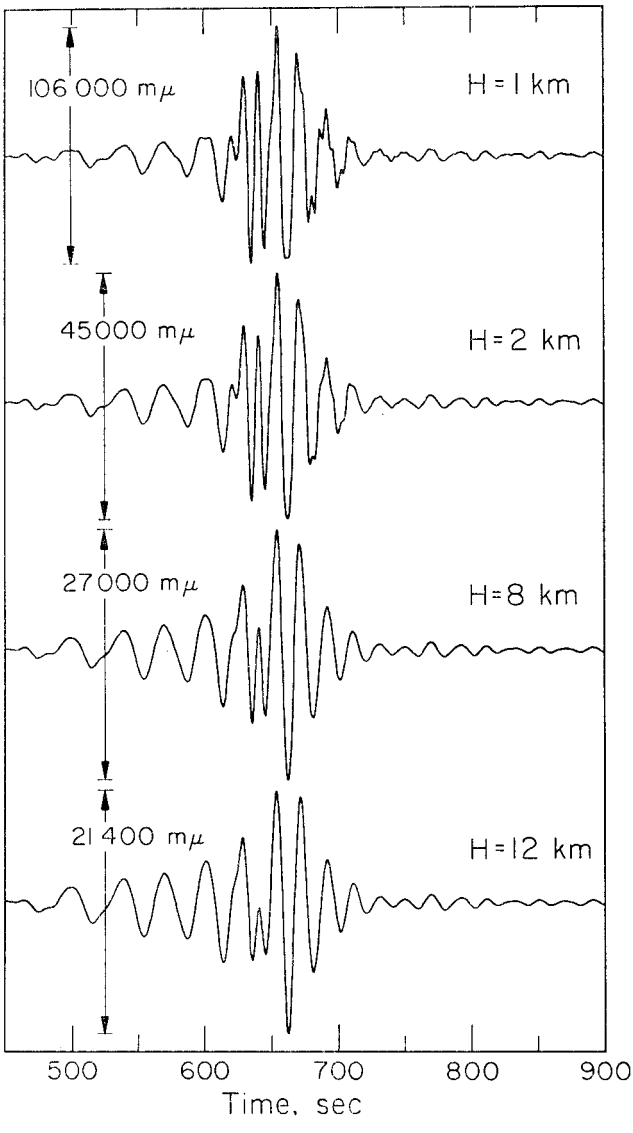

FIG. 19. Synthetic Rayleigh waves for various source depths.

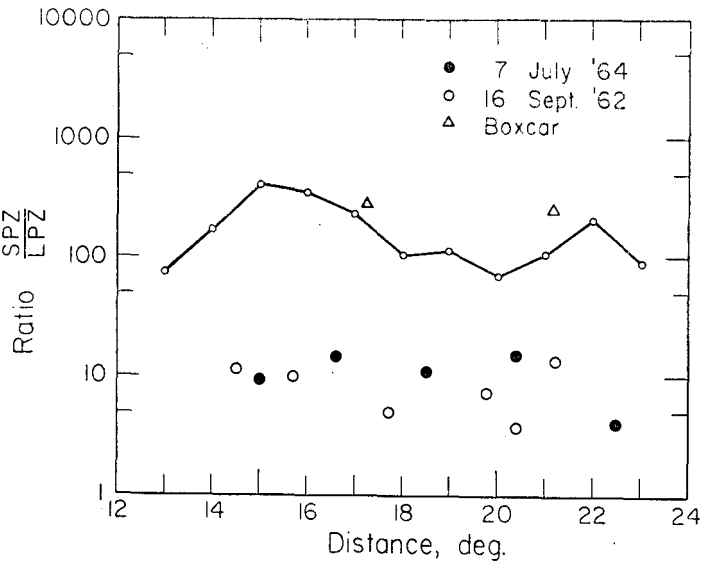

FIG. 20. Theoretical ratio of short- to long-period amplitudes at various ranges. Data from two earthquakes are plotted for comparison.

zones. Each amplitude SPZ and LPZ is divided by its period and adjusted for frequency dependent instrumental magnification following the conventional LRSM shot report descriptions. The two Boxcar points, PGBC and RKON, are in good agreement with the other large explosions. It should be noted that the PGBC point is near the theoretical point at 17°. This feature is just a check on our ability to model the source with our stated assumptions. We expect that points for smaller explosions, yields less than a megaton, to plot above this curve. Points below this curve are either earthquakes or deep explosions. We are assuming that the depth of hypocentre of earthquakes is considerably greater than 1 km and that any radiation pattern will strengthen LPZ by creating a strong P or a strong pP but not both. As discussed earlier we explain the relatively weak long-period P waves from explosions by assuming a symmetric source and allowing pP to cancel P. We included another relatively high stress drop earthquake, Kern (see Fig. 1), occurring in California for comparison.

Conclusions

A source function appropriate for megaton explosions was derived by matching observations with synthetics. Both short- and long-period LRSM recordings were used. Since the long-period seismic signals beyond 30° are quite weak we used the signals near 20°, taking advantage of the amplification produced by the strong velocity gradient in the upper mantle. The complications in seismic signals produced by the structure was handled by the application of generalized ray theory as discussed in the Appendix.

The weakest point in the inversion of these observations is the lack of knowledge concerning the absorption structure. We assumed that the LVZ produces the dominant effect with a net reduction in teleseismic short-period amplitude (1-s period) to 20 per cent of the no absorption level. We further assumed a reduced displacement potential of the form $\phi = \phi_0 t^{\xi} \exp(-\eta t)$. The inversion of the Boxcar observations produced $\phi_0 = 5{\cdot}1 \times 10^5\ \mathrm{m}^3$, $\xi = 0{\cdot}5$ and $\eta = 0{\cdot}15$ assuming t expressed in seconds. Various types of observations including Rayleigh and PL waves were used as a check on the

validity of this source function. However, this solution is non-unique and is strongly dependent on the assumed Q structure, especially at the high frequency limits. No attempt was made in modelling the rise time dependence on yield or the effect of source material. Instead, we concentrated on synthetic behaviours of SPZ and LPZ as the source depth is increased. The interaction between P and pP has a very strong effect on both components, but especially LPZ, since these two arrivals have opposite signs and are comparable in amplitude for idealized explosions detonated in soft materials. Earthquakes are not likely to have this balance in P, pP, and sP and are probably deeper than explosions as well. Thus we would expect that the ratio of SPZ/LPZ to be considerably smaller for earthquakes as compared to explosions. This hypothesis proved valid for a few problem earthquakes, that is earthquakes that cannot be separated from explosions by the m_b *vs.* M_s test. However, using SPZ/LPZ as a discriminate has some strong limitations; namely, the ability to measure long-period amplitudes. This does not appear to be difficult for $m_b > 5$ earthquakes and just determining the ratio to be less than 10 is strong evidence against a shallow explosive source. Of course many events would have to be examined before this discriminate is properly tested.

Acknowledgments

The authors were assisted by Gladys Engen and Shirley Fisher in the computations and digitization of seismograms. This research was supported by the Advanced Research Projects Agency of the Department of Defence and was monitored by the Air Force Office of Scientific Research under Contract Nos. F44620-69-C-0067 and F44620-70-C-0120.

Seismological Laboratory,
California Institute of Technology,
Pasadena, California 91109

References

Carpenter, E. W., 1967. Teleseismic signals calculated for underground, underwater, and atmospheric explosions, *Geophysics.*, **32,** 17–32.

Diment, W. H., Stewart, S. W. & Roller, J. C., 1961. Crustal structure from the Nevada Test Site to Kingman, Arizona from seismic and gravity observations, *J. geophys. Res.*, **66,** 201–214.

Gilbert, F. J. & Helmberger, Donald, V., 1972. Generalized ray theory for a layered sphere, *Geophys. J. R. astr. Soc.*, **27,** 57–80.

Harkrider, D. G., 1964. Surface waves in multilayered elastic media, 1. Rayleigh and Love waves from buried sources in a multilayered elastic half-space, *Bull. seism. Soc. Am.*, **54,** 627–679.

Haskell, N. A., 1967. Analytic approximation for the elastic radiation from a contained underground explosion, *J. geophys. Res.*, **72,** 2582–2587.

Helmberger, D., 1968. The crust–mantle transition in the Bering Sea, *Bull. seism. Soc. Am.*, **52,** 299–319.

Helmberger, Donald V., 1972. Long period wave propagation from 4 to 13°, *Bull. seism. Soc. Am.*, **62,** 325–341.

Helmberger, Donald V. & Morris, Gerald B., 1970. A travel time and amplitude interpretation of a marine refraction profile: transformed shear waves, *Bull. seism. Soc. Am.*, **60,** 593–600.

Helmberger, Donald V. & Wiggins, Ralph A., 1971. Upper mantle structure of midwestern United States, *J. geophys. Res.*, **76,** 3229–3245.

Hoop, A. de, 1960. A modification of Cagniard method for solving seismic pulse problems, *Appl. Sci. Res. B.*, **8,** 349–356.

Johnson, Lane R., 1967. Array measurements of *P* velocity in the upper mantle, *J. geophys. Res.*, **72**, 6309–6325.

Kogeus, Kaj, 1968. A synthesis of short-period *P*-wave records from distant explosion sources, *Bull. seism. Soc. Am.*, **58**, 663–680.

Liebermann, R. C. & Pomeroy, Paul W., 1969. Relative excitation of surface waves by earthquakes and underground explosions, *J. geophys. Res.*, **74**, 1575–1590.

Molnar, Peter, 1971. *P*-wave spectra from underground Nuclear Explosions, *Geophys. J. R. astr. Soc.*, **23**, 273–286.

Stauder, William, 1971. Smaller aftershocks at the Benham nuclear explosion, *Bull. seism. Soc. Am.*, **61**, 417–428.

Strick, E., 1959. Propagation of elastic wave motion from an impulsive source along a fluid–solid interface, Parts II and Parts III, *Phil. Trans. R. Soc. Lond., Ser. A*, **251**, 465–523.

Toksöz, M. N., Ben-Menahem, A. & Harkrider, D. G., 1964. Determination of source parameters of explosions and earthquakes by amplitude equalization of seismic surface waves, *J. geophys. Res.*, **69**, 4355–4366.

Werth, G. C. & Herbst, Roland F., 1963. Comparison of amplitudes of seismic waves from nuclear explosions in four mediums, *J. geophys. Res.*, **68**, 1463–1475.

Wiggins, Ralph & Helmberger, Donald V., 1972. Upper mantle structure of Western United States, *J. geophys. Res.*, in press.

Wyss, M., Hanks, T. C. & Liebermann, R. C., 1971. Comparison of *P*-wave spectra of underground explosions and earthquakes, *J. geophys. Res.*, **76**, 2716–2729.

Appendix

For a spherically symmetrical source in an infinite medium the radial displacement can be expressed in terms of the displacement as

$$u_R(R,t) = \frac{\partial}{\partial R}\phi\left(t-\frac{R}{V}\right) \tag{1}$$

where

$$\phi(R,t) = \psi_0 \frac{F\left(t-\frac{R}{V}\right)}{R}. \tag{2}$$

R is the radial co-ordinate and V is the velocity. The parameter ψ_0 is a constant with units of volume and the function F is the source time dependence. Taking the Laplace transform of (2) yields

$$\bar{\phi}(R,s) = \psi_0 \frac{\bar{F}(s)\exp\left[-(R/V)\,s\right]}{R} \tag{3}$$

where s is the transform variable. Equations (3) can be expressed in cylindrical co-ordinates as

$$\bar{\phi}(r,z,s) = \psi_0 \frac{\bar{F}(s)}{\pi} 2s\,\mathcal{I}m \int_c^{c+i\infty} K_0(spr)\exp\left(-s\eta|z|\right)\frac{p}{\eta}\,dp \tag{4}$$

where

$$\eta = \left(\frac{1}{V^2}-p^2\right)^{\frac{1}{2}}$$

(see Strick 1959 or Helmberger 1968 for details). Substituting the asymptotic form of the modified Bessel function

$$K_0(spr) = \sqrt{\left(\frac{\pi}{2spr}\right)}\exp\left(-spr\right) \tag{5}$$

into (4) we obtain

$$\bar{\phi}(r,z,s) = \psi_0 s\bar{F}(s)\sqrt{\left(\frac{2}{sr\pi}\right)}\,\mathscr{I}m\int_c^{c+i\infty}\frac{\sqrt{p}}{\eta}\exp\left(-s(pr+\eta|z|)\right)dp \tag{6}$$

which can be treated by line source theory (see de Hoop 1960). The solution becomes

$$\phi(r,z,t) = \psi_0\frac{\partial}{\partial t}\left(F(t) * G(t)\right) \tag{7}$$

where $*$ denotes the convolution operation and

$$G(t) = \sqrt{\left(\frac{2}{r}\right)}\frac{1}{\pi}\frac{1}{\sqrt{t}} * \mathscr{I}m\left(\frac{\sqrt{p}}{\eta}\frac{dp}{dt}\right) \tag{8}$$

$G(t)$ is to be evaluated along the complex contour defined by $t = pr+\eta z$. An approximate solution of (8) for large r is

$$G(t) \doteqdot \frac{1}{R}H\left(t-\frac{R}{v}\right) \tag{9}$$

and substitution back into (7) yields the original definition (2) as a check on our technique. As r becomes small more terms in the asymptotic series must be included or the exact solution used. The approximation (5) will suffice for our calculations concerning SPZ and LPZ beyond 12°.

The solution written in operator form as in (7) and (8) is easily extended to handle wave propagation in models containing vertical structure by the application of generalized ray expansions. The further generalization to pulse propagation in a layered sphere is treated by Gilbert & Helmberger (1972) and will not be reproduced here except to clarify how the curvature is handled in this particular application. If we assume a larger number of layers (how large will be discussed later) we can rewrite (8) for a layered sphere as

$$G(t) = \sqrt{\left(\frac{2}{x}\right)}\frac{1}{\pi}\left(\frac{\Delta}{\sin\Delta}\right)^{\frac{1}{2}}\left[\frac{1}{\sqrt{t}} * J(t)\right] \tag{10}$$

where

$$J(t) = \mathscr{I}m\sum_j\frac{\sqrt{p}}{\eta_1}\left(\frac{dp}{dt}\right)_j\Pi(R_j\,T_j) \tag{11}$$

$\Pi(R_j\,T_j)$ is the product of all generalized transmission and reflection coefficients encountered by the ray with index j. Δ is the separation of the source and receiver in radians and x is the arc distance along the surface. Equation (11) is to be evaluated along the de Hoop contour defined by

$$t = px+2\Sigma Th_j\eta_j \tag{12}$$

after applying the Earth flattening approximation. That is

$$\begin{aligned} Th_j &= (r_j-r_{j-1})\,r_0/r_{aj} \\ \alpha_j &= (V_j\,r_0/r_{aj}) \\ \beta_j &= (S_j\,r_0/r_{aj}) \\ \rho_j &= (D_j\,r_0/r_{aj}) \\ r_{aj} &= (r_j+r_{j-1})/2. \end{aligned}$$

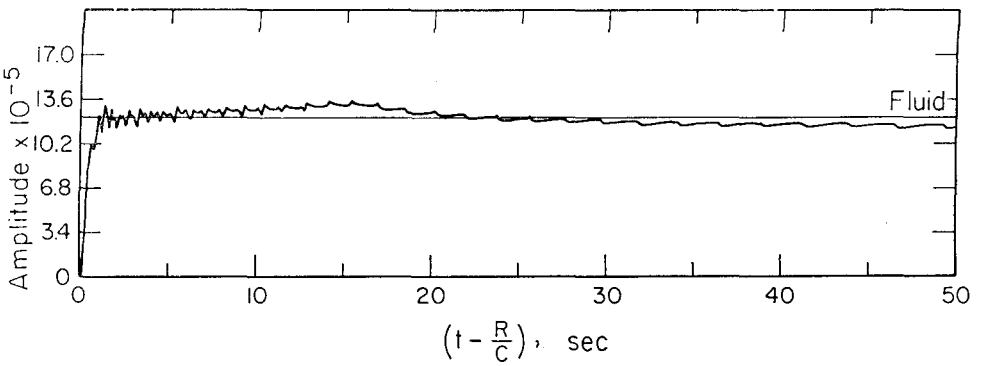

FIG. 21. Comparison of exact solution with numerical approximation.

where r_0 is the radius of the Earth and V, S, D are the velocities and density before transformation. By assuming a larger number of layers we can neglect the contribution from internal multiples and sum only over primary rays, rays that contain one reflection. As a check on this rather involved procedure suppose we generate a synthetic response for the direct wave in a homogeneous wholespace by decomposing the space into spherical shells. Position the source and receiver at $r = 6371$ km with a separation of $\Delta = 80°$. Let $\psi_0 = 1$, $V = 3\,\mathrm{km\,s^{-1}}$ and the density $D = 1$. Assume $f(t) = H(t)$, a step function of unit magnitude so that the exact answer is a step in time arriving at $t = 2733$ s with amplitude $1/R$ or $1{\cdot}22 \times 10^{-4}$. R is just the chord length. Suppose we now replace the homogeneous sphere (space defined by $r < 6371$ km) by spherical shells, each shell having a thickness of 20 km. After applying the Earth flattening approximation we can compute the synthetic response by summation of the primary rays using expressions (11), (10) and (7). The results are given in Fig. 21. The individual peaks are reflections from the various interfaces. At the start of the response these reflections are near critical angle and are coming from depths near the geometrical bottoming depths. Further on in the response the peaks are wide-angle reflections coming from interfaces at shallower depths. The error between the synthetic step function response and the exact is rather complicated. The comparison over the first few seconds is rather severe but this is caused by not taking a sufficient number of layers for short period modelling. The comparison after convolving with the LPZ LRSM response is quite good, only a few per cent difference. It should be realized that this particular model is rather difficult to compute since we are required to turn the wavefront around by gradual means. Our accuracy in generating synthetic models for upper mantle models is probably better than that indicated by Fig. 21.

The vertical displacement at the surface is obtained from the potentials in the conventional manner yielding.

$$u(x,t) = \psi_0 \frac{\partial}{\partial t}\left(F(t) * G(t)\right) \tag{13}$$

where

$$G(t) = \frac{\partial}{\partial t}\left[\sqrt{\left(\frac{2}{x}\right)}\frac{1}{\Pi}\left(\frac{\Delta}{\sin\Delta}\right)^{\frac{1}{2}}\frac{1}{\sqrt{t}} * J(t)\right] \tag{14}$$

and

$$J(t) = \mathscr{I}m \sum_j \left[\frac{2(\eta_\beta^2 - p^2)}{R(p)} \sqrt{p} \left(\frac{dp}{dt} \right)_j \Pi_j(T_j R_j) \right] \tag{15}$$

$R(p)$ is the Rayleigh denominator defined by $R(p) = \beta^2[(\eta_\beta^2 - p^2)^2 + 4p^2 \eta_\alpha \eta_\beta]$ and these functions are evaluated along contours defined by (12). Synthetic seismograms are then computed by a convolution with the appropriate instrument response.